Energy & Environmental Science

ROYAL SOCIETY OF CHEMISTRY

PAPER

View Article Online
View Journal | View Issue

Cite this: *Energy Environ. Sci.*, 2023, **16**, 2316

Revealing the underlying solvent effect on film morphology in high-efficiency organic solar cells through combined *ex situ* and *in situ* observations†

Ruijie Ma, ‡[a] Xinyu Jiang, ‡[b] Jiehao Fu,[a] Tao Zhu,[a] Cenqi Yan,[a] Kexin Wu,[b] Peter Müller-Buschbaum *[bd] and Gang Li *[ac]

The morphological features and the film formation processes in high-performance donor–acceptor binary photovoltaic blends cast from three representative solvents are carefully investigated and analyzed. The PM6:L8-BO system shows a very significant efficiency change on varying the solvent from chloroform (CF) to chlorobenzene (CB) and *o*-xylene (XY), whereas the PM6:eC9 system shows limited influence of the solvent used. *Ex situ* characterization studies have revealed that CB and XY cause too-pronounced phase separation for PM6:L8-BO. In contrast, PM6:eC9 films display only slightly enhanced phase segregation in CB films and even better mixing in XY-processed films. The *in situ* observations further reveal that the PM6 aggregation-dominated stage during film formation is longer for the eC9 system than for L8-BO, effectively suppressing the separation of donors and acceptors. PM6 is found to be highly miscible with the acceptors when processed from XY. The *ex situ* analysis results correlate well with the device performance and are finely explained by the *in situ* and miscibility study. Furthermore, an excellent device efficiency of 19.10% (verified 18.77%) is achieved using a ternary design for XY-enabled organic solar cells (OSCs) with PTQ10, while the corresponding blade coating devices present an excellent PCE of 18.25%. Thereby, this work provides a clear understanding of film morphology formation and enables the realization of high-performance non-halogenated solvent-processed OSCs.

Received 30th January 2023,
Accepted 3rd April 2023

DOI: 10.1039/d3ee00294b

rsc.li/ees

Broader context

Solvent selection is of great significance when polymer donors with remarkable temperature dependent aggregation (TDA) properties are used since such donors have not yet been produced in the field of organic solar cells (OSCs). Since the polymer donors with TDA in the solution state are used in OSC active layer deposition, the morphology tuning can be well addressed once the solubility of small molecular acceptors (SMAs) is appropriate. Accordingly, state-of-the-art PM6:BTP-series systems shall have similarly high efficiencies irrespective of the processing solvent used. However, only chloroform (CF) can be considered a consistently safe choice for them, while non-halogenated solvents (industrially favored) lead to inferior results from time to time. Driven by these unstudied phenomena, we select two representative high-efficiency systems PM6:eC9 and PM6:L8-BO as the research objects, and process corresponding devices with three solvents. Although L8-BO is well-dissolved in all solvents, its chlorobenzene (CB) and *ortho*-xylene (XY) processed devices suffer from serious efficiency loss, while eC9's devices are generally efficient. Subsequent *ex situ* and *in situ* morphology characterization studies reveal the differences in donor–acceptor intermixing in different solvent processing scenarios kinetically and thermodynamically. Guided by a well understood spin-coating morphology evolution, the XY (a high boiling point non-halogenated solvent) enabled blade-coating devices exhibit cutting-edge efficiencies, which opens up new possibilities for printable OSC fabrication.

[a] *Department of Electronic and Information Engineering, Research Institute for Smart Energy (RISE), Guangdong-Hong Kong-Macao (GHM) Joint Laboratory for Photonic-Thermal-Electrical Energy Materials and Devices, The Hong Kong Polytechnic University, Hung Hom, Kowloon, Hong Kong, 999077, China. E-mail: gang.w.li@polyu.edu.hk*

[b] *Lehrstuhl für Funktionelle Materialien, Physik Department, Technische Universität München, James-Franck-Str. 1, 85748 Garching, Germany. E-mail: muellerb@ph.tum.de*

[c] *The Hong Kong Polytechnic University Shenzhen Research Institute, Shenzhen, 518057, China*

[d] *Heinz Maier-Leibnitz Zentrum (MLZ), Technische Universität München Lichtenbergstr. 1, 85748 Garching, Germany*

† Electronic supplementary information (ESI) available. See DOI: https://doi.org/10.1039/d3ee00294b

‡ Equal contribution.

Introduction

Due to the successful boosting of the power conversion efficiency (PCE) to over 19% in single-junctions and over 20% in tandem architectures, organic solar cells (OSCs) are expected to make significant strides in the global photovoltaic (PV) market.[1–11] Today, laboratory progress in OSCs heavily relies on materials design and the research community continues to generate new donor and acceptor materials, to realize higher PCEs that can guarantee the competitiveness of OSCs against other PV technologies. From the aspect of device engineering, the halogenated solvent chloroform (CF) is usually the preferred choice for processing new materials due to its excellent solubility.[12–18] However, CF exhibits high toxicity and carcinogenicity, which seriously challenges its large-scale use.[19,20] Moreover, the low boiling point (BP) characteristics of CF also challenge the solar cell fabrication process. Thus, using non-halogenated solvents with high BPs is highly recommended for establishing large-scale ambient fabrication of OSCs in the future.

The most common processing solvents for state-of-the-art OSC systems, such as CF, chlorobenzene (CB), and xylene (XY) have different BPs, vapor pressures and solubilities. Thus, the film drying processes vary from one solvent to another, resulting in a differently tuned morphology.[21–28] Therefore, understanding the observed PCE variations must be substantiated by an in-depth morphology analysis, enabled by advanced characterization methods including *ex situ* and *in situ* technologies.[29–37] Furthermore, a tight connection between morphological features and device performance needs to be established.[38–40]

Herein, we chose two representative high-PCE photovoltaic systems, namely, PM6:eC9 and PM6:L8-BO,[41,42] processed from CF, CB and XY, respectively, to study the film morphology and device performance in a systematic manner. (full name of the materials is shown in the ESI†). PM6 is selected as the donor material due to its good solubility and featured pre-aggregation in the precursor, while eC9 and L8-BO are two non-fullerene acceptors that showed record PCEs when paired with PM6 in the literature.[41,42] CF and CB are both halogenated solvents, which offer similar solubilities, whereas their BP difference leads to different film formation processes. For XY (non-halogenated), the BP is similar to that of CB. Consequently, the efficiencies of PM6:eC9 processed from CF, CB and XY are 17.79%, 17.52% and 18.16%, respectively. The respective PCE values of PM6:L8-BO are 18.31%, 15.79% and 16.75%. These results show that changing the solvent does not apparently affect the PV performances of the eC9 based system, but significantly alters the PCEs of the L8-BO based devices. The *ex situ* morphology study reveals that both material systems cast from CF exhibit the morphology characteristics of a well miscible phase distribution and interpenetrating networks with long and thick nanofibers. The CB and XY processed films show an increased level of polymer aggregation and donor/acceptor phase separation, but eC9 based active layers display morphological features that are more similar to those of CF processed ones, compared to that of the L8-BO based counterparts. Although the film drying durations for different systems processed using the same solvents are identical, the aggregation behaviors of PM6 and the two NF acceptors are quite different when high BP solvents are used: the PM6 aggregation dominated duration is shorter, and the acceptor aggregation dominated period is longer in the PM6:L8-BO system, compared to PM6:eC9. Therefore, a less intermixing film morphology will be established. Further experimental results suggest that the miscibility of PM6:eC9 is better than that of PM6:L8-BO, which is beneficial for maintaining a favorable intermixing morphology during longer evaporation times. In view of the excellent PCE achieved in the case of PM6:eC9 films processed from the non-halogenated solvent XY, the known ternary blend construction strategy of introducing PTQ10 is applied to achieve even higher PCEs.[43,44] In the case of 20% PTQ10, by substituting PM6 in the blend, a further improved PCE of 19.10% is realized, one of the best PCEs of OSC devices processed from eco-friendly solvents reported so far (verified PCE 18.77% by an independent organization). Meanwhile, corresponding blade coating devices developed by advanced methods of reversing and N_2 knife assisted solidification also achieve a decent efficiency of 18.25%. Therefore, on one hand this study is meaningful in understanding the solvent effect on thin film morphologies and device efficiency, and on the other hand it is an encouraging attempt of combining *ex situ* and *in situ* studies to elucidate the morphology evolution.

Results and discussion

The chemical structures of PM6, eC9 and L8-BO are shown in Fig. 1a together with the processing solvents CF, CB and XY, which have BPs of 61.2 °C, 132 °C, and 144 °C, respectively. Accordingly, when spin coating is used for film deposition, CF processed solutions tend to evaporate quickly, while the CB and XY-based solutions require a longer time to form the solid active layers. Kinetically, the prolonged film drying time can result in a different aggregation behavior of the donor and acceptor materials.

We make a series of OSCs for CF, CB and XY processed PM6:eC9 and PM6:L8-BO systems based on the conventional device structure of ITO/PEDOT:PSS-TA (tyramine doped)/active layers/PFN-Br-MA (melamine doped)/Ag.[45,46] The optimal current density *vs.* voltage (*J*–*V*) characteristics and the external quantum efficiency (EQE) spectra are shown in Fig. S1 (ESI†). The numerical statistics from 20 independent devices for each type of active layer are presented in Fig. S2, S3 and Table S1 (ESI†). A detailed comparison based on averaged open-circuit voltage (V_{OC}), short-circuit current density (J_{SC}), fill factors (FFs) and PCE values is summarized in Fig. 1b. Accordingly, the PCE variation as a function of the processing solvent is insignificant for PM6:eC9 blends compared with PM6:L8-BO ones. The PCE of CF processed PM6:eC9 OSCs is 17.79%, which is consistent with previous reports.[41] In the case of CB, the PCE of PM6:eC9 is 17.52%, with a higher V_{OC} and FF, but a lower J_{SC}. Notably,

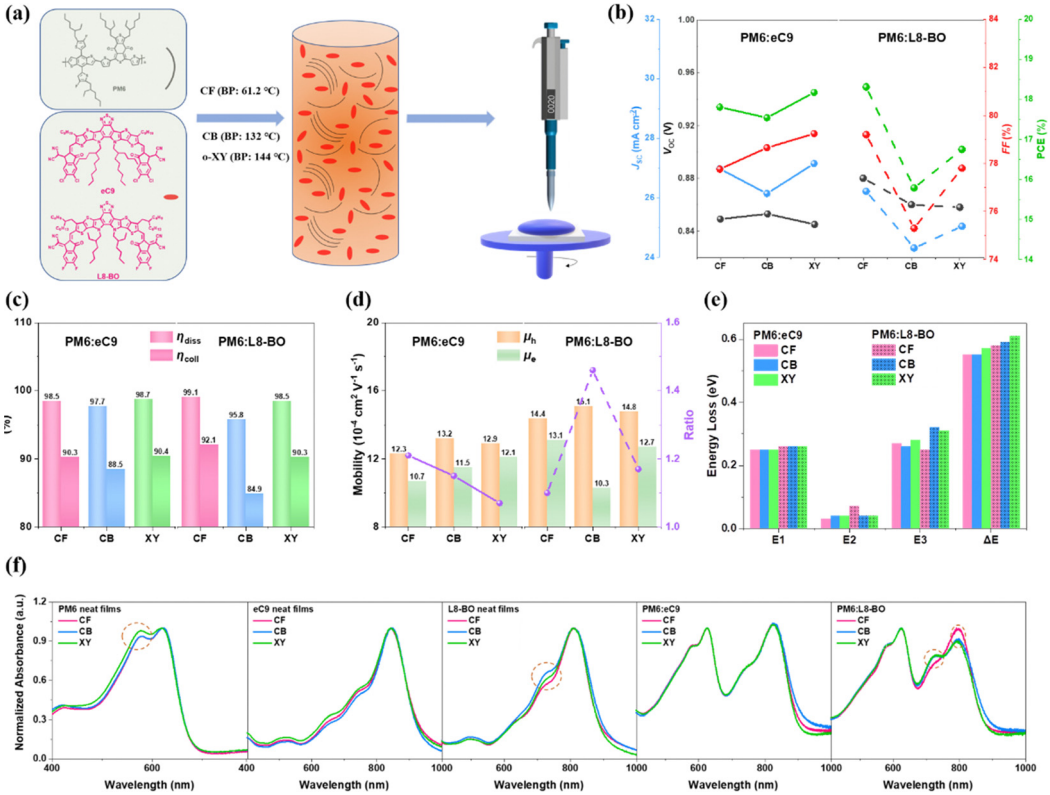

Fig. 1 (a) Chemical structures of donor and acceptors, processing solvents, mixing solution state, and spin coating sketch. (b) V_{OC}, J_{SC}, FF and PCE average values of CF, CB and XY processed devices based on PM6:eC9 and PM6:L8-BO. (c) Calculated values of charge generation and collection rates for the investigated systems. (d) μ_h and μ_e values and their ratios for each system. (e) Energy loss summary. (f) Thin film UV-vis absorption spectra of PM6, eC9, L8-BO, and their blends.

the best PCE is achieved for XY-processed devices, reaching values as high as 18.16%, which is a state-of-the-art value for binary OSCs fabricated using non-halogen solvents. Despite the lowest V_{OC}, XY-processed devices have outstanding J_{SC} and FF values. Moreover, the CF-processed devices based on PM6:L8-BO blends display an optimal PCE of 18.31%, with the best V_{OC}, J_{SC} and FF values, in comparison with its CB- and XY-processed counterparts. The lowest efficiency values for PM6:L8-BO blends are found when CB is used, where all three parameters V_{OC}, J_{SC} and FF are reduced. In the case of XY-processed OSCs, a distinguishable efficiency is reached due to higher J_{SC} and FF values. The results from these device studies match well with the integrated external quantum efficiency (EQE) spectra, which suggests that the errors are below 3%.

Next, we investigate the photocurrent density (J_{ph}) *vs.* effective voltage (V_{eff}) relationships to evaluate the charge dissociation and collection of each system under investigation. The results are plotted in Fig. S4, and the analysis method is also elaborated in the ESI.† The derived η_{diss} and η_{coll} values are presented in Fig. 1c. The CB-processed PM6:L8-BO films are significantly poorer herein. In addition, the bimolecular recombination rates are evaluated by fitting the slope of J_{SC} and illumination intensity in logarithmic presentation, as seen in Fig. S5 (ESI†). The slopes of CF-, CB- and XY-processed PM6:eC9 and PM6:L8-BO based OSCs are 0.96, 0.98, 0.97 and 0.95, 0.97, 0.97, respectively, implying that the use of a high BP solvent can reduce the bimolecular recombination. Such a behavior can probably be attributed to the increased phase separation induced by the high BP solvent. Subsequently, the charge transport characteristics of all types of devices are evaluated by assessing the hole and electron mobilities (μ_h, μ_e) through the space charge limited current (SCLC) method. Hole-only and electron-only device *J*–*V* curves with the logarithmic *x*-axis and *y*-axis are presented in Fig. S6 and S7 (ESI†), together with the corresponding slope curves, which ensures that the data are from the SCLC region.[1] The determined μ_h, μ_e and μ_h/μ_e values are shown in Fig. 1d. The variation tendency of μ_h/μ_es is consistent with the corresponding FFs. Note that the highest μ_h value is achieved by CB-processed films and the lowest μ_e values are achieved by CF-processed films for both photoactive systems, implying that the aggregation behavior of PM6 is dominated by the processing solvent. Furthermore, since the V_{OC} variations of both systems are different, with a drastic drop in the case of CB- and XY-processed PM6:L8-BO based devices, we carry out energy loss analysis on all of them.[47] The Fourier transform photocurrent spectroscopy external quantum efficiency (FTPS-EQE) and electroluminescence (EL) spectra are given in Fig. S8 (ESI†), and EQE_{EL} as a function of the applied current is shown in Fig. S9 (ESI†). The results of ΔE_1 (Shockley–Queisser loss), ΔE_2 (radiative loss below the band gap) and ΔE_3 (non-radiative loss) are calculated and summarized in Fig. 1e.

Apparently, the severe energy reduction in CB- and XY-processed PM6:L8-BO based solar cells is caused by significantly increased ΔE_3 of 0.32 eV and 0.31 eV, compared with the other 4 blends (0.25–0.28 eV). The detailed data can be also found in Table S2 (ESI†).

A variation of the processing solvent will definitely tune the morphology of the active layer to a different degree. However, in the present study, the device efficiency variation trends are complicated and non-monotonous with the order of rising BPs for the two studied systems. Therefore, an in-depth study of the morphology is needed to establish a structure–property correlation. First, the ultraviolet-visible (UV-vis) absorption spectra of neat PM6, eC9, L8-BO and their respective blend films are recorded, to have a general comparison of the aggregation. As seen in Fig. 1f, the CF- and CB-processed PM6 films show identical absorption profiles, while the XY-processed film has a slightly higher 0–1 vibrational shoulder peak. Therefore, although the evaporation process is longer, the aggregation motif cannot be changed by using CB instead of CF, whereas a stronger H-aggregation is enabled by using XY. In the case of neat acceptor films, for the three studied solvents, the eC9 films display no clear difference in the UV-vis spectra, while the L8-BO films exhibit a distinguishable shoulder peak height difference, which is in the following order: CB > XY > CF. The PM6:eC9 blend films show three identical absorption spectra irrespective of the used solvent, indicating that the solvent does not affect the general aggregation motif thoroughly. In contrast, the PM6:L8-BO blend films processed from CB and XY have a significantly lower 0–0 peak and a higher 0–1 peak. This observation suggests that the longer evaporation process has significantly changed the morphology from a favorable to an unfavorable one, when taking the device performance into account. This issue will be sophisticatedly analyzed in a later part, *via* various characterization studies.

The first concern of morphology analysis is the donor–acceptor phase separation, for which a quantitative illustration is enabled by grazing incidence small-angle X-ray scattering (GISAXS) experiments.[48–50] The 2D GISAXS data are presented in Fig. 2a, and horizontal line cuts in the Yoneda region of the active layer are shown in Fig. S10 (ESI†). To model the lateral structures of the active layer, cylindrical and spherical objects with different radii are used in the framework of the distorted wave Born approximation (DWBA) assuming the effective interface approximation (EIA).[51] Three domain structures of different length scales and intensities are extracted from the fits and shown in Fig. 2b and c, respectively. The large domain radii (over 60 nm) represent aggregates inside the active layer, with the apparent lowest intensity distribution across all radii observed in the case of the CF-processed active layer. Thus, GISAXS reveals that the CF solvent favors donor and acceptor mixing. Domains on the order of ten nanometers exhibit structural dimensions, which are suitable in size for splitting excitons into separate charge carriers.[52,53] Therefore the small radii (under 10 nm) plays an important role, when judging the active layer quality. For PM6:eC9 blends, the CB cast film has the highest proportion not only in the small radii but also in the large and medium radii scales, suggesting a strong phase segregation, that could undermine the charge carrier transport to some extent. The reduction of medium radii in XY-processed films, as well as the intensity, implies that XY provokes donor–acceptor intermixing more than CF for PM6:eC9. On the other hand, CF-processed PM6:L8-BO films also have a dominant small-scale phase with 5.8 nm size, and a minor ratio of medium sized domains. These four blend films are generally

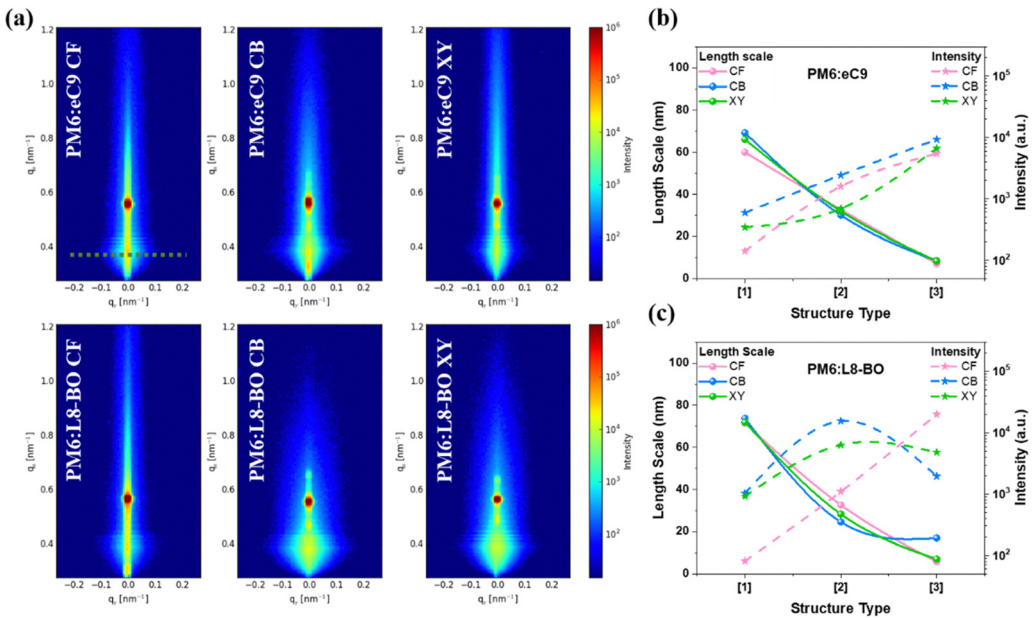

Fig. 2 (a) 2D GISAXS data, the green dash line represents the critical angle of the active layer materials. Nano-structure domain radii and intensities for type [1] (large), [2] (medium), [3] (small) structures of (b) PM6:eC9 and (c) PM6:L8-BO systems.

of similar type concerning their phase distribution, which refers to an efficiency-favorable one. However, a drastic change happens in CB-processed PM6:L8-BO films: the medium structure radii intensity becomes 15 times stronger than that of the small structure radii, which suggests that the film morphology undergoes transition from highly intermixed to a strong phase separation. A similar tendency is observed in the XY-processed PM6:L8-BO films, but the intensity difference between medium and small structures is not that severe (about 9 times). This finding means that the XY-processed films exhibit a morphology with milder phase separation than the undesired CB-processed PM6:L8-BO.

The above results are also substantiated by the direct observations in the transmission electron microscopy (TEM) images, as shown in Fig. S11 (ESI†). The CF-processed films of both, PM6:eC9 and PM6:L8-BO, possess a well-mixed donor–acceptor phase, which is beneficial for charge generation. Moreover, they show distinguishable long and narrow fibrils (pure phase), and well mixed bright and dark phases with small length scales, which is consistent with GISAXS calculation results. In the case of PM6:L8-BO films cast from CB and XY, a significant phase self-aggregation is observed (CB > XY), so their GISAXS results are directly supported. As for CB and XY processed eC9 based blend films, the general feature of phase separation observed from images is very similar – also consistent with GISAXS data. It is somehow understandable that longer drying times result in a more significant phase separation between the donor and acceptor materials. However, in PM6:eC9 blend films, the situation is completely different. Starting from the solvent CF, well mixed and interpenetrating multi-length scale features are enabled. Only CB-processed films have a slightly enhanced phase segregation that corresponds to its J_{SC} loss in the respective devices. The ideal morphology re-appears in the XY-processed films, which is consistent with the increased J_{SC} and FF values, but requires further explanation. We acknowledge that the TEM image comparison here is not significant enough, which is in essence reasonable for preaggregation property of PM6, but this part of study can be a solid side-evidence for the already precise quantitative analysis of GISAXS.

The film crystallinity, as a result of the material crystallization behavior, is further studied using the grazing incidence wide-angle X-ray scattering (GIWAXS) technique.[54–56] Shown in Fig. 3a and b are 2D GIWAXS data and the related cake cuts in the in plane (IP) and out-of-plane (OOP) directions. The related fit parameters are summarized in Tables S3–S5 (ESI†). The (100) peak representing the PM6 lamellar diffraction exhibits a 20.9 Å *d*-spacing for all PM6:eC9 films irrespective of the solvent and for CF-processed PM6:L8-BO films. A reduced value of 20.2 Å is found for CB- and XY-processed PM6:L8-BO films. The coherence length (CL) values for them are 57.7, 79.7, 58.3, 71.6, 52.9 and 51.4 Å, orderly. For the (010) peak that reflects π–π stacking properties, the *d*-spacing values are 3.72 Å, 3.72 Å, 3.74 Å for eC9 and 3.74 Å, 3.72 Å, 3.70 Å for L8-BO systems when processed from CF, CB, XY, and the corresponding CL values of these peaks are17.0, 18.2, 17.0, 18.9, 18.5 and 18.6 Å, respectively. These results demonstrate the independent crystallization of donor and acceptor materials in a lamellar packing and π–π stacking scenario when using different solvents studied here. In contrast, the co-crystallization varies

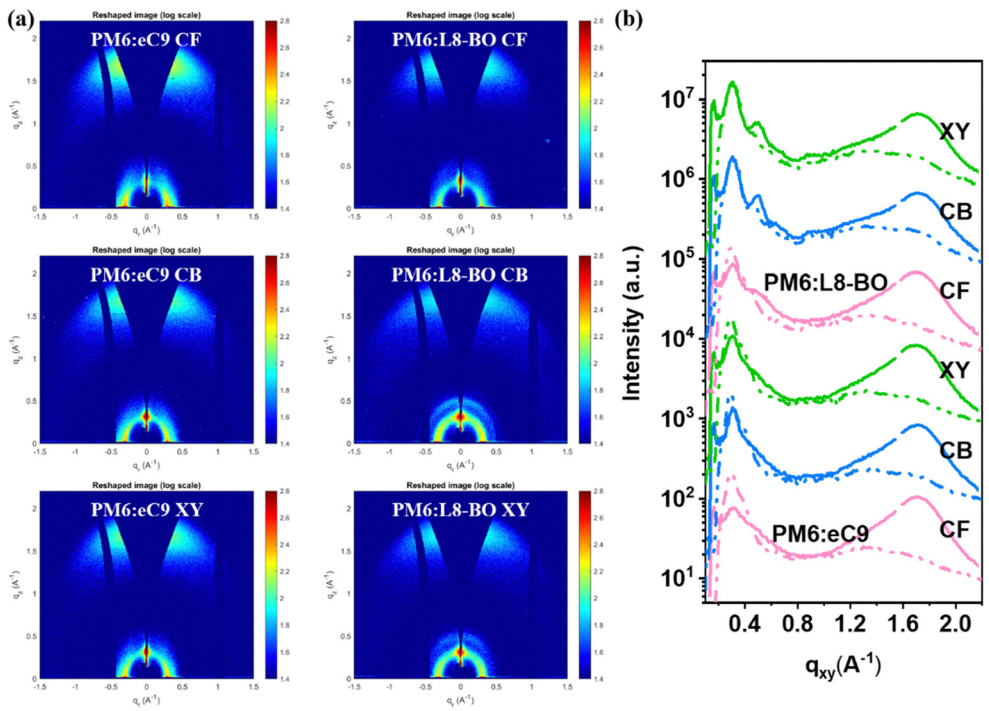

Fig. 3 (a) 2D GIWAXS data and (b) corresponding cake cuts in the IP (dash) and OOP (solid) direction.

significantly from solvent to solvent for the investigated systems. Compared with the PM6:eC9 films, the PM6:L8-BO-CF films show a decelerated intensity reduction from $\sim$0.4 Å^{-1} to $\sim$0.6 Å^{-1} irrespective of the processing solvent, since L8-BO tends to form its own nano-fibrils and forms a bi-continuity network.[1] In addition, CB-processed PM6:L8-BO films display an additional peak located at $\sim$0.49 Å^{-1} along the OOP direction, corresponding to a CL of 91.2 Å ($\sim$7 consecutive crystallites). This indicates that a large amount of L8-BO is separated from the PM6 phase, since the original co-crystallization is broken. Besides, the XY-processed L8-BO films also demonstrate a similar peak ($\sim$0.47 Å^{-1}) with a weaker intensity, which has a very small CL of 7.1 Å. This finding indicates the incomplete independent crystallization in the lamellar region or in other words, a recovered co-crystallization and intermixing to some extent. To gain deeper insights into the orientation distribution of the crystallites, we perform tube cuts from the 2D GIWAXS data in a q range of 0.2 to 0.4 Å^{-1}, which is along the (100) peak. The percentage of edge-on, face-on, and isotropic oriented crystallites calculated by integrating the areas of the corresponding features in the pole figures (corrected $I(\chi) \times \sin(\chi)$ *vs.* χ plots) is shown in Fig. S12, S13 and Table S6 (ESI†). For PM6:eC9 thin films, the face-on orientation of the crystallites covers 81.7%, 63.3% and 59.9% and the isotropic orientation is 18.0%, 35.2%, 39.4% when processed from CF, CB and XY, respectively. Thus, we find a face-on-dominated orientation in the PM6:eC9 thin films, which provides favorable conditions for the charge carrier pathway in OSCs. Similarly, a face-on-dominated orientation is also confirmed in the PM6:L8-BO films processed from CF representing 63.1% of the crystallites and the isotropic orientation is 36.5%. However, an increased isotropic orientation of 58.8% and 54.3% dominates the crystallites in the CB- and XY-processed PM6:L8-BO thin films, respectively. Such dominating isotropic orientations hinder the charge carrier transport in these blend thin films. However, despite having a higher percentage of isotropic orientation in the XY processed PM6:eC9 samples, they show better donor and acceptor intermixing than those processed with CF (confirmed by GISAXS), and they show the best device performance.

To elucidate the similarities and dissimilarities of the morphology variation tendencies as a function of the processing solvent, we study the film formation process. With time dependent-photoluminescence (PL), we can observe and analyze the various stages of film drying, material aggregation, and the film formation processes.[57–59] In Fig. 4, the contour maps of the PL intensities are shown for systems considered in the present study, with their main peak position, intensity and total area values. The whole drying process is divided into three stages, which are marked as purple, blue and green regions. In addition, the gray region refers to the substrate spinning before the start of the solution coating. Both the investigated systems show a very quick and linear decrease in the PL integrated peak areas in the case of CF-processing, which means that the donor and acceptor aggregate and crystallize together. Such behavior is beneficial for maintaining the initial intermixing morphology. In the case of the high BP solvent drying processes, the solvent evaporation clearly shows two stages, based on the

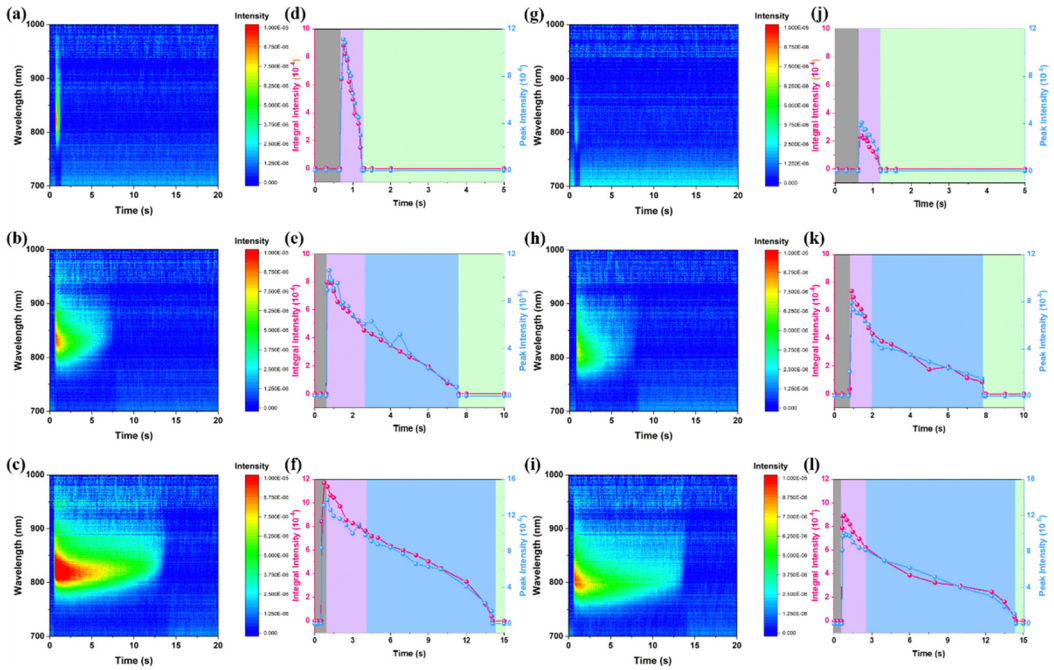

Fig. 4 Contour maps of time resolved PL spectra for the PM6:eC9 system cast from (a) CF, (b) CB and (c) XY; corresponding calculated parameters in the case of (d) CF, (e) CB and (f) XY. Contour maps of time resolved PL spectra for PM6:L8-BO system cast from (g) CF, (h) CB and (i) XY; corresponding calculated parameters in the case of (j) CF, (k) CB and (l) XY. Gray region: before spin coating; purple region: polymer aggregation dominated stage; blue region: small molecule aggregation domination; and green region: main solvent is completely removed.

change in the peak intensity and integrated area curve slopes. The purple region shows a fast drop in the integral intensity signals due to an enhancement and distance reduction of the chromophores. This trend results from the polymer aggregation (major contribution) and from the small molecule precipitation (minor contribution). Within the blue region, the integral PL peak areas decrease with a slower speed, indicating the completion of the polymer aggregation and of the formation of a network structure. Therefore, this stage is dominated by small molecule aggregation and crystallization, since its solubility is better and its aggregation tendency is weaker than that of the polymer. We note that in the present study, the PM6 dominated aggregation stage is obviously shorter in the PM6:L8-BO system compared with PM6:eC9 systems, although the total durations of the CB- and XY-processed film drying processes are almost identical for both. Thus, L8-BO separates from PM6 in the liquid phase more quickly than eC9 does. Accordingly, the CB- and XY-processed PM6:L8-BO films display a larger phase segregation morphology, which is not observed in the corresponding PM6:eC9 films. Furthermore, an interesting phenomenon in the blue region of XY related films is noticed. In the blue region for NFA dominated drying, a faster signal drop at tail is observed for XY systems, while rather monotonic intensity reduction occurs in CF and CB ones. Guided by the previous literature, we assign this phenomenon to the role of DIO additives.[60] When the ratio of DIO reaches a certain level, the acceptor will be induced to aggregate even during the process of liquid-to-solid transition, which can lead to a slight increase in emission. This result explains the slower signal decrease in XY than in CB in most parts of the blue region. It is supported by the fact that the DIO's molar ratio in XY main solvent is higher than in CB. At the end of the blue stage, all chromophores quickly get quenched due to complete drying.

After figuring out the underlying reason for the enlarged phase separation in PM6:L8-BO films when using BP solvent processing, our next target is to understand the morphology recovery in the XY-films. Thus, a miscibility assessment is carried out based on contact angle experiments.[61,62] The neat films of PM6, eC9 and L8-BO processed from the three solvents studied here are exposed to water and ethylene glycol (EG) droplets. The formed droplets are displayed in Fig. S14 (ESI†). The determined surface tensions are presented in Fig. 5a–c, based on two different algorithms. Fig. 5d plots the related interaction (miscibility) parameters accordingly.[63,64] It is found that the miscibility parameters are at a similar level for PM6 *vs.* eC9 and PM6 *vs.* L8-BO in the CF and CB processed films, meaning that the enlarged phase separation is mainly due to the film drying kinetics. XY-processed PM6 and L8-BO films also indicate a similar miscibility (slightly lower). Therefore, the recovery degree of the XY-processed film morphologies is limited. Moreover, we can see that PM6 and eC9 are highly miscible with each other as well, so the highly mixed donor–acceptor distribution in their blend films is well explained.

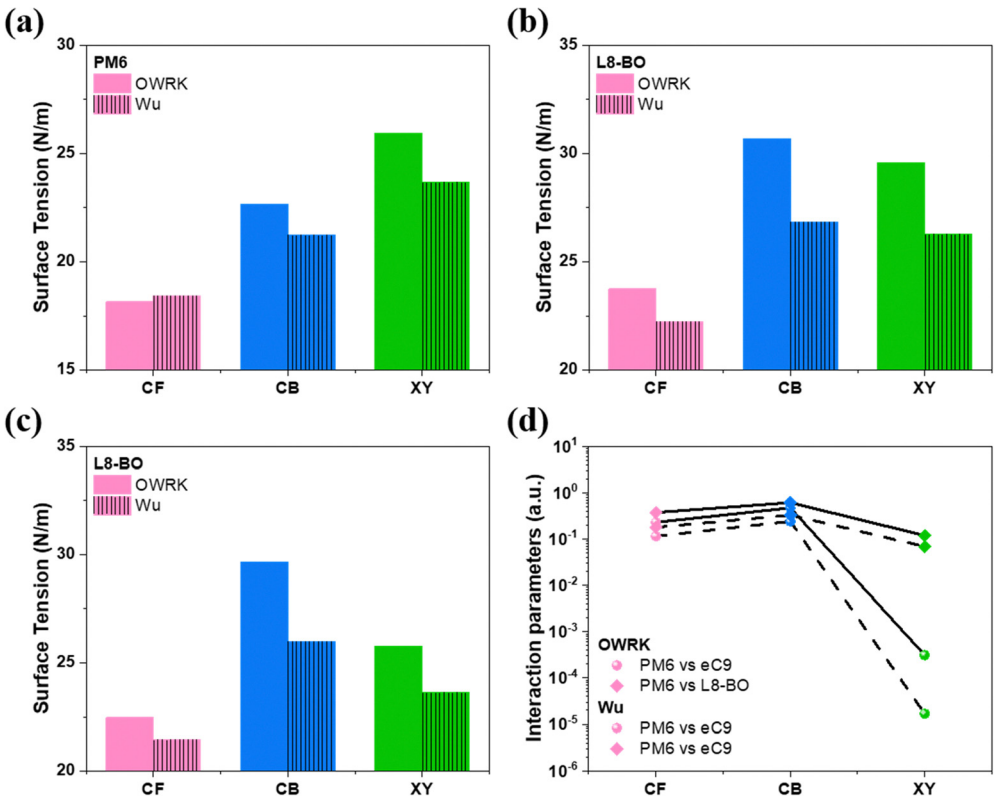

Fig. 5 Surface tensions of PM6, eC9 and L8-BO neat films from different solvents calculated using two algorithms (Wu and OWRK models), and deduced interaction (miscibility) parameters.

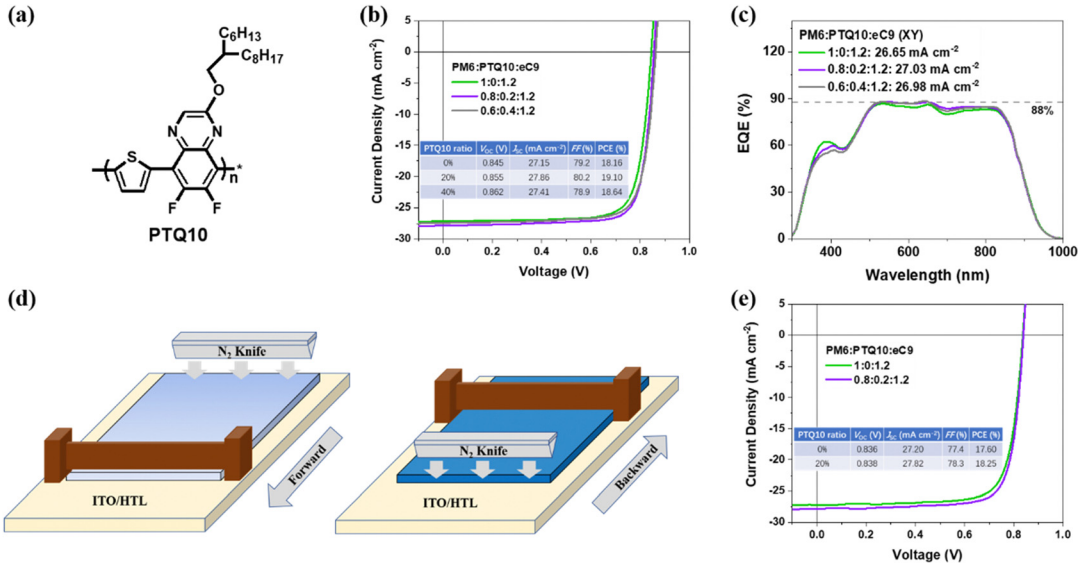

Fig. 6 (a) Chemical structure of PTQ10. (b) *J*–*V* characteristics. (c) EQE spectra. (d) Schematic diagram of blade coating and (e) *J*–*V* characteristics.

In addition, these findings also demonstrate why CF is often a preferred choice in device optimization when new materials are introduced. Based on its low BP and fast evaporation kinetics, photoactive materials regardless of being polymers or small molecules are going to intermix with each other well during the initial blending in the liquid phase, and a subsequent aggregation or crystallization can be finely tuned by post treatments such as annealing and the use of volatile additives. Moreover, the material selection principle for gaining high-efficiency eco-friendly solvent processed OSCs can be preliminarily established. The principle is that the material–material–solvent interaction in the solution state shall deliver a well miscible morphology in the initially cast films. As for further optimization, there is still room for enhancing crystallinity and phase separation; post treatments (solvent additive, thermal annealing, solvent vapor fumigation *etc.*) can be employed to achieve the desired film morphology.

Another interesting point worth discussion is to correlate the relationship between morphology features and V_{OC}. A simple claim is that over-separated phases without enough nanofibrils such as CB and XY processed PM6:L8-BO active layers suffer great loss in both V_{OC} and J_{SC}, but one noticeable issue is that CB type PM6:eC9 has larger phase separation while achieving higher V_{OC} than its CF and XY counterparts. Considering this point, we suppose that the slightly enlarged phase separation only causes loss in J_{SC}, but nothing negative to V_{OC} and FF, which is also widely observed in the whole field as a result of properly increased phase purity.

Importantly, binary solar cells based on PM6:eC9 can show a PCE over 18%, when processed from XY, which is an encouraging result for eco-friendly solvent processed OSCs. A further efficiency enhancement is pursued by the ternary strategy – PM6:PTQ10:eC9. An increase in PCE is expected from the synergy between PM6 and PTQ10, in combination with the fact that PTQ10 can be well dissolved by XY as well. The chemical structure of PTQ10 is given in Fig. 6a. The related photovoltaic parameters of the studied ternary devices with varied compositions are shown in Fig. 6b as *J*–*V* characteristics with the characteristic parameters shown in the inserted table. The best efficiency of 19.10% is achieved by selecting 20% of PTQ10, which demonstrates an appealing advance in the progress of OSCs.[65–72] For completeness, the EQE spectra of these devices are also provided in Fig. 6c. To provide context of our findings, Fig. S15 (ESI†) presents a brief comparison of our result with other reported non-halogenated solvent processed OSC devices reported in literature. Details are given in Table S7 (ESI†). For further confirmation, an independent third-party certification upon this result is carried out and presented in Fig. S16 (ESI†).

Furthermore, the importance of non-halogenated solvent's utilization is for printing compatible film coatings, so the open-air blade coating devices based on PM6:eC9 and optimal PM6:PTQ10:eC9 systems were fabricated with N_2-knife assisted coating.[73–77] The schematic diagram is drawn in Fig. 6d, while the photovoltaic parameters and *J*–*V* curves of the devices are shown in Fig. 6e (EQE spectra in Fig. S17, ESI†). The efficiencies obtained are as high as 17.60% and 18.25% for binary and optimal ternary blend systems, respectively. Such results are also among the highest values reported for blade coating to date.

Conclusion

In summary, motivated by the popular solvent choice (CF) for device fabrication in recent OSC works, and considering large-scale fabrication solvent requirements (moderately high BP), we studied a series of devices based on two high-efficiency systems (PM6:eC9 and PM6:L8-BO) by selecting three representative solvents: CF, CB and XY. Comprehensive *ex situ* and *in situ* investigations along with device data allowed us to recognize

the favorable morphology with an intermixing phase distribution and a nano-fibril formed network. Moreover, the ideal film formation process is identified, *i.e.*, having a fast solvent evaporation, which leaves no time for an undesired to strong phase separation. Furthermore, the successful PCE improvement in XY-processed PM6:eC9 based OSCs and the miscibility study suggest that achieving high-efficiency in similar types of systems would also require that the donor and acceptor materials are highly miscible. A well-developed ternary matrix is built to boost the efficiency of non-halogenated solvent enabled OSCs (both spin and blade coating), which results in very high values. Therefore, this work demonstrates comprehensively combined *ex situ* and *in situ* investigations, resolves several morphological issues, and provides in depth understanding and suggestions for a further development of OSC's material and device engineering.

Author contributions

Ruijie Ma: conceptualization, investigation, formal analysis, writing – original draft, methodology, and validation; Xinyu Jiang: investigation, formal analysis, methodology, and writing – original draft; Jiehao Fu: validation; Tao Zhu: investigation; Cenqi Yan: investigation; Kexin Wu: investigation; Peter Müller-Buschbaum: resources, supervision, writing – review and editing, and funding acquisition; Gang Li: resources, supervision, writing – review and editing, and funding acquisition.

Conflicts of interest

The authors declare no conflict of interest.

Acknowledgements

G. L. acknowledges the support from the Research Grants Council of Hong Kong (project No. 15221320 and C5037-18G), the RGC Senior Research Fellowship Scheme (SRFS2223-5S01), the Shenzhen Science and Technology Innovation Commission (JCYJ20200109105003940), the Hong Kong Polytechnic University Internal Research Funds: Sir Sze-yuen Chung Endowed Professorship Fund (8-8480), RISE (Q-CDA5), G-SAC5, 1-YW4C and the Guangdong-Hong Kong-Macao Joint Laboratory for Photonic-Thermal-Electrical Energy Materials and Devices (GDSTC No. 2019B121205001). P.M.B appreciates the support from the Deutsche Forschungsgemeinschaft (DFG, German Research Foundation) grant no. Mu1487/22, the International Research Training Group 2022 Alberta/Technical University of Munich International Graduate School for Environmentally Responsible Functional Hybrid Materials (ATUMS) and under Germany's Excellence Strategy – EXC 2089/1 – 390776260 (e conversion), TUM. solar in the context of the Bavarian Collaborative Research Project Solar Technologies Go Hybrid (SolTech) and the Center for NanoScience (CeNS). R. M. is thankful for the PolyU distinguished Postdoctoral Fellowship. X. J. acknowledges the financial support from the Chinese Scholarship Council (CSC). Dr Wei Gao of the City University of Hong Kong is appreciated for the help with device performance verification.

References

1 L. Zhu, M. Zhang, J. Xu, C. Li, J. Yan, G. Zhou, W. Zhong, T. Hao, J. Song, X. Xue, Z. Zhou, R. Zeng, H. Zhu, C.-C. Chen, R. C. I. MacKenzie, Y. Zou, J. Nelson, Y. Zhang, Y. Sun and F. Liu, *Nat. Mater.*, 2022, **21**, 656–663.
2 Y. Cui, Y. Xu, H. Yao, P. Bi, L. Hong, J. Zhang, Y. Zu, T. Zhang, J. Qin, J. Ren, Z. Chen, C. He, X. Hao, Z. Wei and J. Hou, *Adv. Mater.*, 2021, **33**, 2102420.
3 L. Zhan, S. Li, Y. Li, R. Sun, J. Min, Y. Chen, J. Fang, C.-Q. Ma, G. Zhou, H. Zhu, L. Zuo, H. Qiu, S. Yin and H. Chen, *Adv. Energy Mater.*, 2022, 2201076.
4 W. Gao, F. Qi, Z. Peng, F. R. Lin, K. Jiang, C. Zhong, W. Kaminsky, Z. Guan, C.-S. Lee, T. J. Marks, H. Ade and A. K. Y. Jen, *Adv. Mater.*, 2022, **34**, 2202089.
5 R. Ma, C. Yan, J. Yu, T. Liu, H. Liu, Y. Li, J. Chen, Z. Luo, B. Tang, X. Lu, G. Li and H. Yan, *ACS Energy Lett.*, 2022, **7**, 2547–2556.
6 Y. Wei, Z. Chen, G. Lu, N. Yu, C. Li, J. Gao, X. Gu, X. Hao, G. Lu, Z. Tang, J. Zhang, Z. Wei, X. Zhang and H. Huang, *Adv. Mater.*, 2022, **34**, 2204718.
7 K. Chong, X. Xu, H. Meng, J. Xue, L. Yu, W. Ma and Q. Peng, *Adv. Mater.*, 2022, **34**, 2109516.
8 R. Sun, Y. Wu, X. Yang, Y. Gao, Z. Chen, K. Li, J. Qiao, T. Wang, J. Guo, C. Liu, X. Hao, H. Zhu and J. Min, *Adv. Mater.*, 2022, **34**, 2110147.
9 G. Liu, R. Xia, Q. Huang, K. Zhang, Z. Hu, T. Jia, X. Liu, H. L. Yip and F. Huang, *Adv. Funct. Mater.*, 2021, **31**, 2103283.
10 Z. Zheng, J. Wang, P. Bi, J. Ren, Y. Wang, Y. Yang, X. Liu, S. Zhang and J. Hou, *Joule*, 2022, **6**, 171–184.
11 Y. Huang, L. Meng, H. Liang, M. Li, H. Chen, C. Jiang, K. Zhang, F. Huang, Z. Yao, C. Li, X. Wan and Y. Chen, *J. Mater. Chem. A*, 2022, **10**, 11238–11245.
12 Y. Shi, Y. Chang, K. Lu, Z. Chen, J. Zhang, Y. Yan, D. Qiu, Y. Liu, M. A. Adil, W. Ma, X. Hao, L. Zhu and Z. Wei, *Nat. Commun.*, 2022, **13**, 3256.
13 C. Zhu, L. Meng, J. Zhang, S. Qin, W. Lai, B. Qiu, J. Yuan, Y. Wan, W. Huang and Y. Li, *Adv. Mater.*, 2021, **33**, 2100474.
14 Z. Luo, R. Ma, J. Yu, H. Liu, T. Liu, F. Ni, J. Hu, Y. Zou, A. Zeng, C.-J. Su, U. S. Jeng, X. Lu, F. Gao, C. Yang and H. Yan, *Nat. Sci. Rev.*, 2022, **9**, nwac076.
15 Z. Luo, Y. Gao, H. Lai, Y. Li, Z. Wu, Z. Chen, R. Sun, J. Ren, C. E. Zhang, F. He, H. Woo, J. Min and C. Yang, *Energy Environ. Sci.*, 2022, **15**, 4601–4611.
16 L. Zhu, M. Zhang, G. Zhou, T. Hao, J. Xu, J. Wang, C. Qiu, N. Prine, J. Ali, W. Feng, X. Gu, Z. Ma, Z. Tang, H. Zhu, L. Ying, Y. Zhang and F. Liu, *Adv. Energy Mater.*, 2020, **10**, 1904234.
17 T. Xu, J. Lv, K. Yang, Y. He, Q. Yang, H. Chen, Q. Chen, Z. Liao, Z. Kan, T. Duan, K. Sun, J. Ouyang and S. Lu, *Energy Environ. Sci.*, 2021, **14**, 5366–5376.

18 S. Li, L. Zhan, N. Yao, X. Xia, Z. Chen, W. Yang, C. He, L. Zuo, M. Shi and H. Zhu, *Nat. Commun.*, 2021, **12**, 1–11.
19 T. A. Jorgenson, E. F. Meierhenry, C. J. Rushbrook, R. J. Bull and M. Robinson, *Fundam. Appl. Toxicol.*, 1985, **5**, 760–769.
20 W. Guan, D. Yuan, J. Wu, X. Zhou, H. Zhao, F. Guo, L. Zhang, K. Zhou, W. Ma and W. Cai, *J. Semi.*, 2021, **42**, 030502–030504.
21 L. Ye, Y. Xiong, Q. Zhang, S. Li, C. Wang, Z. Jiang, J. Hou, W. You and H. Ade, *Adv. Mater.*, 2018, **30**, 1705485.
22 S. Dong, T. Jia, K. Zhang, J. Jing and F. Huang, *Joule*, 2020, **4**, 2004–2016.
23 L. Ye, S. Zhang, W. Ma, B. Fan, X. Guo, Y. Huang, H. Ade and J. Hou, *Adv. Mater.*, 2012, **24**, 6335–6341.
24 R. Ma, T. Yang, Y. Xiao, T. Liu, G. Zhang, Z. Luo, G. Li, X. Lu, H. Yan and B. Tang, *Energy Environ. Mater.*, 2022, **5**, 977–985.
25 Z. Li, L. Ying, P. Zhu, W. Zhong, N. Li, F. Liu, F. Huang and Y. Cao, *Energy Environ. Sci.*, 2019, **12**, 157–163.
26 C. Sprau, F. Buss, M. Wagner, D. Landerer, M. Koppitz, A. Schulz, D. Bahro, W. Schabel, P. Scharfer and A. Colsmann, *Energy Environ. Sci.*, 2015, **8**, 2744–2752.
27 D. Wang, H. Liu, Y. Li, G. Zhou, L. Zhan, H. Zhu, X. Lu, H. Chen and C.-Z. Li, *Joule*, 2021, **5**, 945–957.
28 L. Zhu, W. Zhong, C. Qiu, B. Lyu, Z. Zhou, M. Zhang, J. Song, J. Xu, J. Wang, J. Ali, W. Feng, Z. Shi, X. Gu, L. Ying, Y. Zhang and F. Liu, *Adv. Mater.*, 2019, **31**, 1902899.
29 L. Ye, H. Hu, M. Ghasemi, T. Wang, B. A. Collins, J.-H. Kim, K. Jiang, J. H. Carpenter, H. Li, Z. Li, T. McAfee, J. Zhao, X. Chen, J. L. Y. Lai, T. Ma, J.-L. Bredas, H. Yan and H. Ade, *Nat. Mater.*, 2018, **17**, 253–260.
30 K. Zhou, K. Xian, Q. Qi, M. Gao, Z. Peng, J. Liu, Y. Liu, S. Li, Y. Zhang, Y. Geng and L. Ye, *Adv. Funct. Mater.*, 2022, **32**, 2201781.
31 J. Xin, X. Meng, X. Xu, Q. Zhu, H. B. Naveed and W. Ma, *Matter*, 2019, **1**, 1316–1330.
32 K. Gao, W. Deng, L. Xiao, Q. Hu, Y. Kan, X. Chen, C. Wang, F. Huang, J. Peng, H. Wu, X. Peng, Y. Cao, T. P. Russell and F. Liu, *Nano Energy*, 2016, **30**, 639–648.
33 Z. Peng, L. Ye and H. Ade, *Mater. Horizons*, 2022, **9**, 577–606.
34 S. Engmann, F. A. Bokel, H. W. Ro, D. M. DeLongchamp and L. J. Richter, *Adv. Energy Mater.*, 2016, **6**, 1502011.
35 F. Liu, S. Ferdous, E. Schaible, A. Hexemer, M. Church, X. Ding, C. Wang and T. P. Russell, *Adv. Mater.*, 2015, **27**, 886–891.
36 L. J. Richter, D. M. DeLongchamp and A. Amassian, *Chem. Rev.*, 2017, **117**, 6332–6366.
37 W. Zhong, M. Zhang, G. Freychet, G. M. Su, L. Ying, F. Huang, Y. Cao, Y. Zhang, C. Wang and F. Liu, *Adv. Mater.*, 2022, **34**, 2107316.
38 H. Chen, R. Zhang, X. Chen, G. Zeng, L. Kobera, S. Abbrent, B. Zhang, W. Chen, G. Xu, J. Oh, S.-H. Kang, S. Chen, C. Yang, J. Brus, J. Hou, F. Gao, Y. Li and Y. Li, *Nat. Energy*, 2021, **6**, 1045–1053.
39 R. Ma, K. Zhou, Y. Sun, T. Liu, Y. Kan, Y. Xiao, T. A. Dela Peña, Y. Li, X. Zou, Z. Xing, Z. Luo, K. S. Wong, X. Lu, L. Ye, H. Yan and K. Gao, *Matter*, 2022, **5**, 725–734.
40 T. Hao, W. Zhong, S. Leng, R. Zeng, M. Zhang, L. Zhu, Y. Yang, J. Song, J. Xu, G. Zhou, Y. Zou, Y. Zhang and F. Liu, *Sci. China: Chem.*, 2022, **65**, 1634–1641.
41 Y. Cui, H. Yao, J. Zhang, K. Xian, T. Zhang, L. Hong, Y. Wang, Y. Xu, K. Ma, C. An, C. He, Z. Wei, F. Gao and J. Hou, *Adv. Mater.*, 2020, **32**, 1908205.
42 C. Li, J. Zhou, J. Song, J. Xu, H. Zhang, X. Zhang, J. Guo, L. Zhu, D. Wei, G. Han, J. Min, Y. Zhang, Z. Xie, Y. Yi, H. Yan, F. Gao, F. Liu and Y. Sun, *Nat. Energy*, 2021, **6**, 605–613.
43 L. Arunagiri, Z. Peng, X. Zou, H. Yu, G. Zhang, Z. Wang, J. Y. Lin Lai, J. Zhang, Y. Zheng, C. Cui, F. Huang, Y. Zou, K. S. Wong, P. C. Y. Chow, H. Ade and H. Yan, *Joule*, 2020, **4**, 1790–1805.
44 W. Zhang, C. Sun, I. Angunawela, L. Meng, S. Qin, L. Zhou, S. Li, H. Zhuo, G. Yang, Z.-G. Zhang, H. Ade and Y. Li, *Adv. Mater.*, 2022, **34**, 2108749.
45 R. Ma, M. Zeng, Y. Li, T. Liu, Z. Luo, Y. Xu, P. Li, N. Zheng, J. Li, Y. Li, R. Chen, J. Hou, F. Huang and H. Yan, *Adv. Energy Mater.*, 2021, **11**, 2100492.
46 X. Xiong, X. Xue, M. Zhang, T. Hao, Z. Han, Y. Sun, Y. Zhang, F. Liu, S. Pei and L. Zhu, *ACS Energy Lett.*, 2021, **6**, 3582–3589.
47 Y. Wang, D. Qian, Y. Cui, H. Zhang, J. Hou, K. Vandewal, T. Kirchartz and F. Gao, *Adv. Energy Mater.*, 2018, **8**, 1801352.
48 X. Jiang, P. Chotard, K. Luo, F. Eckmann, S. Tu, M. A. Reus, S. Yin, J. Reitenbach, C. L. Weindl, M. Schwartzkopf, S. V. Roth and P. Müller-Buschbaum, *Adv. Energy Mater.*, 2022, **12**, 2103977.
49 Z. Wang, K. Gao, Y. Kan, M. Zhang, C. Qiu, L. Zhu, Z. Zhao, X. Peng, W. Feng, Z. Qian, X. Gu, A. K. Y. Jen, B. Z. Tang, Y. Cao, Y. Zhang and F. Liu, *Nat. Commun.*, 2021, **12**, 332.
50 D. Yang, F. C. Löhrer, V. Körstgens, A. Schreiber, B. Cao, S. Bernstorff and P. Müller-Buschbaum, *Adv. Sci.*, 2020, **7**, 2001117.
51 X. Jiang, H. Kim, P. S. Deimel, W. Chen, W. Cao, D. Yang, S. Yin, R. Schaffrinna, F. Allegretti, J. V. Barth, M. Schwager, H. Tang, K. Wang, M. Schwartzkopf, S. V. Roth and P. Müller-Buschbaum, *J. Mater. Chem. A*, 2020, **8**, 23628–23636.
52 S. Athanasopoulos, S. Tscheuschner, H. Bässler and A. Köhler, *J. Phys. Chem. Lett.*, 2017, **8**, 2093–2098.
53 M. T. Sajjad, A. Ruseckas and I. D. W. Samuel, *Matter*, 2020, **3**, 341–354.
54 J. Rivnay, S. C. B. Mannsfeld, C. E. Miller, A. Salleo and M. F. Toney, *Chem. Rev.*, 2012, **112**, 5488–5519.
55 H. Zhao, H. B. Naveed, B. Lin, X. Zhou, J. Yuan, K. Zhou, H. Wu, R. Guo, M. A. Scheel, A. Chumakov, S. V. Roth, Z. Tang, P. Müller-Buschbaum and W. Ma, *Adv. Mater.*, 2020, **32**, 2002302.
56 J. Fang, Z. Wang, J. Zhang, Y. Zhang, D. Deng, Z. Wang, K. Lu, W. Ma and Z. Wei, *Adv. Sci.*, 2015, **2**, 1500250.
57 H. Zhao, B. Lin, J. Xue, H. B. Naveed, C. Zhao, X. Zhou, K. Zhou, H. Wu, Y. Cai, D. Yun, Z. Tang and W. Ma, *Adv. Mater.*, 2022, **34**, 2105114.

58 Q. Zhu, J. Xue, G. Lu, B. Lin, H. B. Naveed, Z. Bi, G. Lu and W. Ma, *Nano Energy*, 2022, **97**, 107194.
59 Y. Liu, A. Yangui, R. Zhang, A. Kiligaridis, E. Moons, F. Gao, O. Inganäs, I. G. Scheblykin and F. Zhang, *Small Methods*, 2021, **5**, 2100585.
60 J. Xin, J. Feng, B. Lin, H. B. Naveed, J. Xue, N. Zheng and W. Ma, *Small*, 2022, **18**, 2200608.
61 R. Ma, T. Liu, Z. Luo, K. Gao, K. Chen, G. Zhang, W. Gao, Y. Xiao, T.-K. Lau, Q. Fan, Y. Chen, L.-K. Ma, H. Sun, G. Cai, T. Yang, X. Lu, E. Wang, C. Yang, A. K. Y. Jen and H. Yan, *ACS Energy Lett.*, 2020, **5**, 2711–2720.
62 T. Xu, J. Lv, K. Yang, Y. He, Q. Yang, H. Chen, Q. Chen, Z. Liao, Z. Kan, T. Duan, K. Sun, J. Ouyang and S. Lu, *Energy Environ. Sci.*, 2021, **14**, 5366–5376.
63 D. K. Owens and R. C. Wendt, *J. Appl. Polym. Sci.*, 1969, **13**, 1741–1747.
64 S. Wu, *J. Polym. Sci., Part C: Polym. Symp.*, 1971, **34**, 19–30.
65 Y. Xu, Y. Cui, H. Yao, T. Zhang, J. Zhang, L. Ma, J. Wang, Z. Wei and J. Hou, *Adv. Mater.*, 2021, **33**, 2101090.
66 D. Wang, G. Zhou, Y. Li, K. Yan, L. Zhan, H. Zhu, X. Lu, H. Chen and C.-Z. Li, *Adv. Funct. Mater.*, 2022, **32**, 2107827.
67 H. Lu, H. Wang, G. Ran, S. Li, J. Zhang, Y. Liu, W. Zhang, X. Xu and Z. Bo, *Adv. Funct. Mater.*, 2022, **32**, 2203193.
68 X. Song, P. Sun, D. Sun, Y. Xu, Y. Liu and W. Zhu, *Nano Energy*, 2022, **91**, 106678.
69 R. Sun, T. Wang, Y. Wu, M. Zhang, Y. Ma, Z. Xiao, G. Lu, L. Ding, Q. Zheng, C. J. Brabec, Y. Li and J. Min, *Adv. Funct. Mater.*, 2021, **31**, 2106846.
70 B. Fan, F. Lin, J. Oh, H. Fu, W. Gao, Q. Fan, Z. Zhu, W. J. Li, N. Li, L. Ying, F. Huang, C. Yang and A. K. Y. Jen, *Adv. Energy Mater.*, 2021, **11**, 2101768.
71 J. Wang, Y. Cui, Y. Xu, K. Xian, P. Bi, Z. Chen, K. Zhou, L. Ma, T. Zhang, Y. Yang, Y. Zu, H. Yao, X. Hao, L. Ye and J. Hou, *Adv. Mater.*, 2022, **34**, 2205009.
72 L. Zhan, S. Yin, Y. Li, S. Li, T. Chen, R. Sun, J. Min, G. Zhou, H. Zhu, Y. Chen, J. Fang, C.-Q. Ma, X. Xia, X. Lu, H. Qiu, W. Fu and H. Chen, *Adv. Mater.*, 2022, 2206269.
73 J. Zhang, L. Zhang, X. Wang, Z. Xie, L. Hu, H. Mao, G. Xu, L. Tan and Y. Chen, *Adv. Energy Mater.*, 2022, **12**, 2200165.
74 B. Zhang, F. Yang, S. Chen, H. Chen, G. Zeng, Y. Shen, Y. Li and Y. Li, *Adv. Funct, Mater.*, 2022, **32**, 2202011.
75 Y. Zhang, K. Liu, J. Huang, X. Xia, J. Cao, G. Zhao, P. W. K. Fong, Y. Zhu, F. Yan, Y. Yang, X. Lu and G. Li, *Nat. Commun.*, 2021, **12**, 4815.
76 P. W.-K. Fong, H. Hu, Z. Ren, K. Liu, L. Cui, T. Bi, Q. Liang, Z. Wu, J. Hao and G. Li, *Adv. Sci.*, 2021, **8**, 2003359.
77 Q. Bai, Q. Liang, H. Li, H. Sun, X. Guo and L. Niu, *Aggregate*, 2022, e281.

